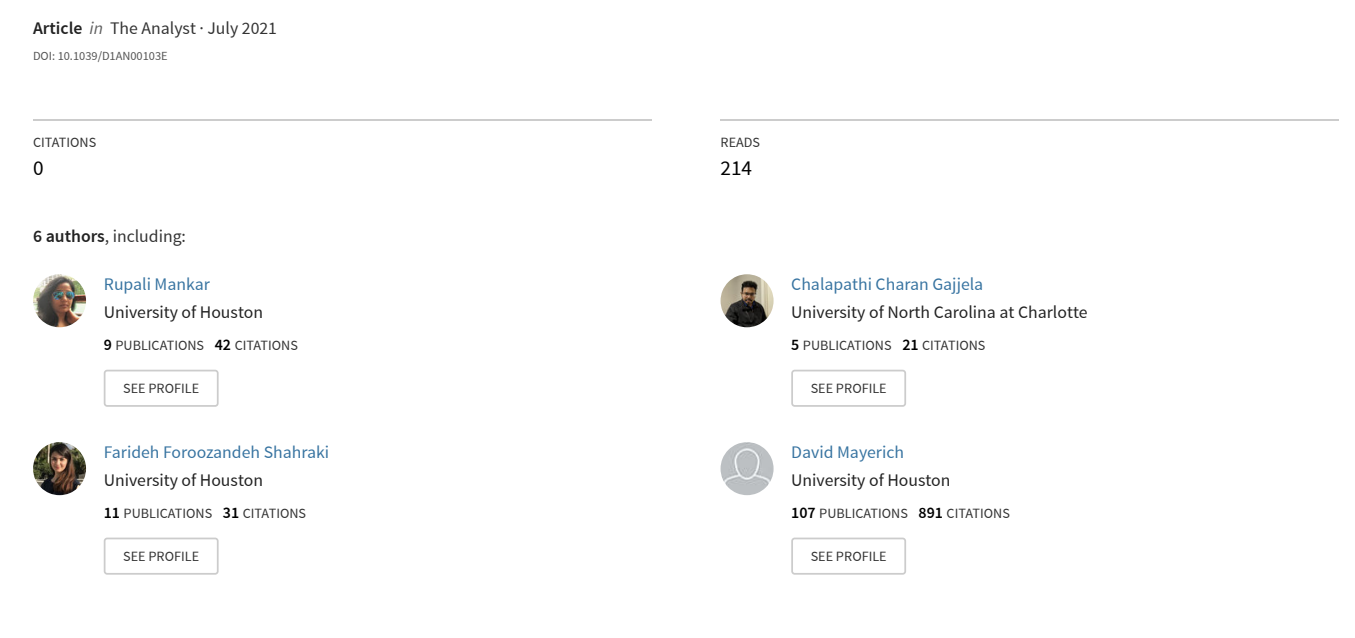
Multi-Modal Image Sharpening in Fourier Transform Infrared (FTIR) Microscopy



Some of the authors of this publication are also working on these related projects:



GRAPH CONVOLUTIONAL NEURAL NETWORKS FOR HYPERSPECTRAL DATA CLASSIFICATION View project





Analyst

Accepted Manuscript

This article can be cited before page numbers have been issued, to do this please use: R. Mankar, C. Gajjela, F. Foroozandeh, S. Prasad, D. Mayerich and R. Reddy, *Analyst*, 2021, DOI: 10.1039/D1AN00103E.



This is an Accepted Manuscript, which has been through the Royal Society of Chemistry peer review process and has been accepted for publication.

Accepted Manuscripts are published online shortly after acceptance, before technical editing, formatting and proof reading. Using this free service, authors can make their results available to the community, in citable form, before we publish the edited article. We will replace this Accepted Manuscript with the edited and formatted Advance Article as soon as it is available.

You can find more information about Accepted Manuscripts in the <u>Information for Authors</u>.

Please note that technical editing may introduce minor changes to the text and/or graphics, which may alter content. The journal's standard <u>Terms & Conditions</u> and the <u>Ethical guidelines</u> still apply. In no event shall the Royal Society of Chemistry be held responsible for any errors or omissions in this Accepted Manuscript or any consequences arising from the use of any information it contains.



6 7 8

9

10 11 ₹2

127:52:5772/6775 tto transfort Cyclesials and passon and 12005 that one companying the companyin

38

39

40

41

42

43

44

45

46

47

48

49

50

51

52

53

54

55

56

57

58 59 60

Journal Name

ARTICLE TYPE

Cite this: DOI: 00.0000/xxxxxxxxxx

Multi-Modal Image Sharpening in Fourier Transform Infrared (FTIR) Microscopy

Rupali Mankar, Chalapathi Charan Gajjela, Farideh Foroozandeh, Saurabh Prasad, David Mayerich, and Rohith Reddy*

Received Date Accepted Date

DOI: 00.0000/xxxxxxxxxx

Mid-infrared Spectroscopic Imaging (MIRSI) provides spatially-resolved molecular specificity by measuring wavelength-dependent mid-infrared absorbance. Infrared microscopes use large numerical aperture objectives to obtain high-resolution images of heterogeneous samples. However, the optical resolution is fundamentally diffraction-limited, and therefore wavelength-dependent. This significantly limits resolution in infrared microscopy, which relies on long wavelengths ($2\,\mu m$ to $12\,\mu m$) for molecular specificity. The resolution is particularly restrictive in biomedical and materials applications, where molecular information is encoded in the fingerprint region ($6\,\mu m$ to $12\,\mu m$), limiting the maximum resolving power to between $3\,\mu m$ and $6\,\mu m$. We present an unsupervised curvelet-based image fusion method that overcomes limitations in spatial resolution by augmenting infrared images with label-free visible microscopy. We demonstrate the effectiveness of this approach by fusing images of breast and ovarian tumor biopsies acquired using both infrared and dark-field microscopy. The proposed fusion algorithm generates a hyperspectral dataset that has both high spatial resolution and good molecular contrast. We validate this technique using multiple standard approaches and through comparisons to super-resolved experimentally measured photothermal spectroscopic images. We also propose a novel comparison method based on tissue classification accuracy.

1 Introduction

Broadband vibrational spectroscopic imaging provides excellent molecular sensitivity that can identify the spatial distribution of molecular constituents. Fourier transform infrared (FTIR) spectroscopic imaging is a popular technique that is used to measure mid-infrared absorbance spectra in materials science, 1,2 forensics, 3 and biomedicine 4,5 by illuminating the sample with mid-infrared (mid-IR) light in the range of 750 to 4000 cm $^{-1}$ (13.3 to 2.5μ m). 6 This technique is commercially available, facilitating wide adoption in settings where *mid-infrared spectroscopic imaging* (MIRSI) is necessary to provide molecular context at each pixel.

The spatial resolution $\Delta \ell$ of an imaging system under the Rayleigh criterion is proportional to the incident wavelength λ and inversely proportional to the objective's numerical aperture NA:

$$\Delta \ell = 0.61 \frac{\lambda}{NA}.\tag{1}$$

The numerical aperture is fixed and usually in the range of \approx 0.5 to 0.8. Spatial resolution is therefore wavelength-dependent and varies significantly (up to 6×) across the mid-IR range

(2.5 to $13.3\mu m$). MIRSI instrument manufacturers typically use pixel sizes between $5 \mu m$ and $7 \mu m$ based on the spatial resolution in the fingerprint region (900 to 1800cm^{-1}). This is sub-optimal for biomedical applications that require sub-cellular resolution to evaluate heterogeneous tissue structures. Recent commercial platforms provide high-definition⁸ imaging that reduces pixel sizes to $\approx 1.1 \,\mu m$ to achieve the best possible spatial resolution. ^{8,9} These advances improve image quality in highwavenumber bands (3000 to 3500cm⁻¹). ¹⁰ However images in the fingerprint region, which encode molecular contrast for a variety of organic molecules, are still diffraction limited. ¹¹ The final images are high resolution at higher wavenumbers, due to the reciprocal relationship to wavelength, while important molecular information at longer wavelengths is obscured in low-resolution images. Methods that improve the spatial resolution at these wavenumbers can significantly improve the viability of FTIR in biomedical applications. ¹²

Resolution limits in MIRSI hinder the analysis of histological samples where small spatial features, such as collagen fibers ($\approx 2\,\mu\mathrm{m}$ wide) and cell clusters, are clinically important. Applications requiring high spatial resolution have motivated the development of new MIRSI instruments leveraging probes to overcome the diffraction limit. $^{13-16}$ Photothermal IR (PTIR) 17 and optical photothermal IR (O-PTIR) 18 enable sub-micrometer resolution

University of Houston, Houston, Texas, USA.

^{*} Email: rkreddy@uh.edu

3

4

MIRSI by training on hematoxylin and eosin (H&E) stained tissue images. This approach has limited applicability in histopathology applications where data consists of several cell types and subtypes, since the spatial enhancement is not uniform for all morphological features but biased towards the morphological features highlighted by H&E.

Pansharpening is used extensively in remote sensing to fuse high-resolution panchromatic images with multispectral (MS) data. 26 This produces images with better spatial and spectral resolution through cost-effective imaging using independent sensors optimized for (1) high spectral resolution (MS sensor) and (2) high spatial resolution (panchromatic sensor). 27 Pansharpening commonly relies on component substitution: a low-resolution hyperspectral (HS) image is projected onto a new basis, such as the one provided by principal component analysis (PCA). Highfrequency components are inserted by replacing elements in the projected basis. The inverse transform is then applied to produce a fused output. Pansharpening with PCA is a component substitution algorithm, ²⁸ where the MS image is transformed using PCA. The first component of the new MS image is replaced by the high-resolution pan image to add spatial detail. Inverting the fused MS projection results in a sharpened MS output. Component substitution techniques are unsupervised, and do not require training or a corresponding ground truth. However, these sharpening techniques are prone to spectral distortion. The extent of these distortions depends on the correlation between the sharp pan band and the replaced component of the projected MS image.

Another approach involves directly injecting spatial details into low-resolution images. These methods separate spatial features using multi-resolution analysis (MRA). Wavelet-based fusion, band dependent spatial injection (BDSD), and waveletbased Bayesian fusion are examples of spatial detail injection methods. ²⁹ These methods provide better spectral fidelity, since the injected features are optimized for each band and there is no upper limit on the number of injected high-resolution bands. Most pansharpening algorithms are supervised. Band dependent spatial detail (BDSD) uses a ground truth image to identify optimal parameters for injecting spatial details. BDSD is also computationally intensive since the inserted spatial features are computed using the entire MS image. ²⁶ Clustered-BDSD (C-BDSD) algorithm is an extension of BDSD algorithm with efficient implementation. C-BDSD optimizes parameters on pixels clustered using spatial features unlike BDSD in which parameters are estimated globally or locally with a sliding window. 30 Parameter estimation on clustered pixels makes C-BDSD fast and accurate when compared to BDSD. Although C-BDSD is fast and works well for remote sensing, it is a supervised algorithm which relies on a high resolution ground truth. The nonavailability of high resolution FTIR hyperspectral images makes supervised approaches impractical.

Spatial-spectral fusion methods using the Fourier or wavelet transforms are good at retaining spectral information at the expense of spatial detail. Wavelet transforms are poor at representing curved edges, making them sub-optimal for microscopic images of organic materials. ³² The curvelet transform is therefore

with simultaneous spectroscopic contrast. While individual band images and spectra can be acquired rapidly using O-PTIR, measuring full hyperspectral cubes is currently too time consuming for routine clinical applications. However, spectroscopic imaging data from O-PTIR provides a direct experimental measurement of sub-micron spatial features and spectroscopic signatures, which is challenging to obtain through other technologies. We use it as a gold standard to assess the technology proposed in the current manuscript.

This paper proposes curvelet-based multi-modal fusion to enhance spatial resolution in chemical maps, bridging the gap between MIRSI and traditional histology to achieve cellular-level resolution with FTIR instrumentation. The proposed method builds on image sharpening techniques from remote sensing ^{19,20} and extends it to mid-IR hyperspectral datasets using a novel unsupervised approach to integrating high-frequency features into hyperspectral images. In remote sensing, low resolution multispectral (MS) images are fused with high-resolution panchromatic (PAN) images. Such sharpening is commonly referred to as pansharpening. Our approach uses dark-field microscopy to obtain high-resolution data analogous to panchromatic images. High spatial frequency features are fused into MIRSI data using an unsupervised curvelet-based approach. This combination of dark-field microscopy and MIRSI provides several practical advantages: (1) both modalities are label-free; (2) high-resolution image acquisition requires very little additional time, and (3) no changes to sample preparation are required. Unlike current photothermal imaging, our technique does not require new instrumentation, or long hyperspectral data acquisition times.

We demonstrate the efficacy of the proposed algorithm on tissue biopsies, where both molecular specificity 21 and cellular-level resolution ($<5\,\mu\text{m}$) 22 are critical to clinical diagnosis but beyond the capabilities of FTIR imaging. We evaluate the efficacy of our fusion algorithm using quantitative metrics, such as spectral distortions relative to the raw hyperspectral data. We also propose evaluations based on classification of the fusion data and comparing these results to both FTIR and traditional histopathology. This novel evaluation method is more practical for MIRSI, since it focuses on optimizing the resulting image for reconstruction, which is currently the most common task in infrared histology.

1.1 Previous Work

Multi-modal image fusion refers to a broad class of techniques combining data from two or more modalities to produce an information-rich output image. This provides clinical insights that each modality cannot furnish alone. Such techniques are common in medical imaging, where magnetic resonance imaging (MRI), computed tomography (CT), positron emission tomography (PET), and single-photon emission computed tomography ²³ are fused to provide a comprehensive data set for a single patient. Multi-modal image fusion can also speed up acquisition. Work by Kong et al. ²⁴ demonstrates that integration of autofluorescence imaging and Raman scattering acquires molecular information faster than the conventional histology. Falahkheirkhah ²⁵ has proposed a deep learning framework to enhance spatial details of

56

57

3

4

5

6

7

8

9

10

11

∄2

38

39

40

41

42

43

44

45

46

47

48

49

50

51

52

53

54

55

56

57

58 59 60 preferred in medical imaging applications, such as image segmentation 33 and fusion. 31

2 Curvelet Transform

The curvelet transform ³⁴ (CT) is an extension of wavelets ³⁵ and ridgelets. ³⁶ Images are decomposed into sub-bands of different scales using the wavelet transform, and then a localized ridgelet transform is applied to each sub-band. Curvelets can represent high-frequency contours at a range of scales using a sparse set of coefficients combined with the curvelet basis. The curvelet transform includes three stages: (1) image decomposition, (2) smooth partitioning, and (3) a ridgelet transform:

- Image decomposition: Each band image is decomposed into resolution-based sub-bands using a 2D isotropic wavelet transform. Each layer contains details of different frequencies.
- 2. Smooth partitioning: The first layer is low frequency and can be smoothly expressed using wavelets. However, the wavelet transform is not efficient for representing high-frequency curved features. High frequency features are therefore represented with curvelets. To represent high-frequency features efficiently using curvelets, each sub-band is divided into square partitions of a size appropriate for the scale (Figure 1). At a finer scale, curved edges are divided into smaller fragments with smaller square partitions and treated as straight edges.
- 3. **Ridgelet transform:** The ridgelet transform is applied on each square partition of each sub-band.

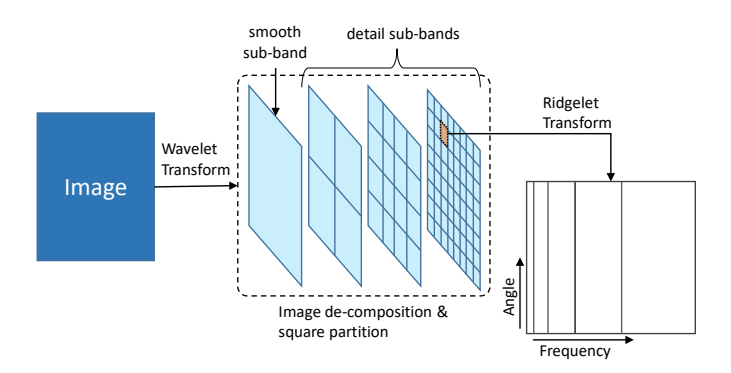


Fig. 1 An illustrtion of the Curvelet transform

The continuous curvelet transform and fast discrete curvelet transform are developed by E.J.Candes et.al.. 37 In this section, we illustrate the utility of curvelet transforms in the context of our proposed image fusion algorithm. A curvelet transform, defined on a two dimensional function f(x,y), is represented using curvelet coefficients computed by taking inner product of elements of f and curvelet at different scales and orientations. In a curvelet transform, φ_j is defined as a mother curvelet. 37 Curvelets at scales 2^{-j} are obtained through rotations and translations of the mother curvelet. At decomposition scale 2^{-j} , orientations of curvelets are given by the sequence of equispaced rotation angles $\theta_l = 2\pi \cdot 2^{-\frac{l}{2}} \cdot l$, with $l = 0, 1, \cdots$ such that $0 < \theta_l < 2\pi$

and translation given by sequence of translation parameters are $k=(k_1,k_2)\in\mathbb{Z}$. At scale 2^{-j} and orientation θ_l and positions $x_k^{(j,l)}=R_{\theta_l}^{-1}(k_1\cdot 2^{-j},k_2\cdot ^{-\frac{j}{2}})$, with R_{θ} is rotation by θ , curvelets are defined (as a function of x) by:

$$\varphi_{j,l,k}(x) = \varphi_j\left(R_{\theta_l}\left(x - x_k^{(j,l)}\right)\right).$$
 (2)

Any function $f \in L^2(\mathbb{R}^2)$ can be represented as a series of curvelet coefficients and a curvelet coefficient at scale 2^{-j} , direction l and location k is computed by taking inner product between an element f and a curvelet $\varphi_{i,l,k}$,

$$c_{j,l,k} = \langle f, \varphi_{j,l,k} \rangle. \tag{3}$$

Function f sparsely represented using discrete curvelet coefficients is reconstructed using formula,

$$f = \sum_{j,l,k} \langle f, \varphi_{j,l,k} \rangle \cdot \varphi_{j,l,k}. \tag{4}$$

The curvelet transform is a multidimensional extension of the wavelet transform, which can effectively represent curved discontinuities with fewer coefficients than wavelets. Medical images are composed of many curved edges optimally represented by wedges using sparse curvelet coefficients. 31,33 The sharpness of the curved edges in a hyperspectral band image changes as a function of wavelengths due to the diffraction. The CT decomposes images into multi-resolution sub-bands representing curved features at different scales and orientation. In Figure 2, curvelet coefficients for two FTIR band images (1080 cm⁻¹ and 1650 cm⁻¹) are shown with the Cartesian concentric corona for the first four scales. The coarse scale is in the center of the corona. The coefficient scale increases from inner to outer corona, with coefficients at different orientations measured clockwise from the top left. Number of angles (orientations) changes with the scale and with the number of angles selected for 2nd coarsest scale which is 16 (Figure 2). The band image at $1650 \,\mathrm{cm}^{-1}$ is sharper than the image at $1080\,\mathrm{cm}^{-1}$, therefore dense coefficients are seen at finer scales corresponding to higher wavenumbers. Multi-resolution sparse decomposition is useful for fusing high spatial frequency features without introducing artifacts into the spectral domain.

3 Materials and Methods

Our curvelet-based multi-modal fusion is validated on 10 tissue samples from breast and ovarian tissue microarrays (TMAs). We procured formalin fixed paraffin embedded (FFPE) breast (AMS802) and ovarian (BC11115c) sections from commercial tissue banks, with adjacent sections placed on IR transparent CaF₂ and standard glass slides. All sections went through the same deparaffinization protocol. Unstained sections on CaF₂ slides were imaged using both FTIR and dark-field microscopes. Adjacent sections on glass were stained with H&E and imaged in brightfield. TMAs included tissue cores from different grades and stages of cancer to enable validation on biochemically diverse tissues. Ten 1 mm cores from each array (10 different patients) were sharpened and annotated to compute the classification accuracy of the two key histological classes.

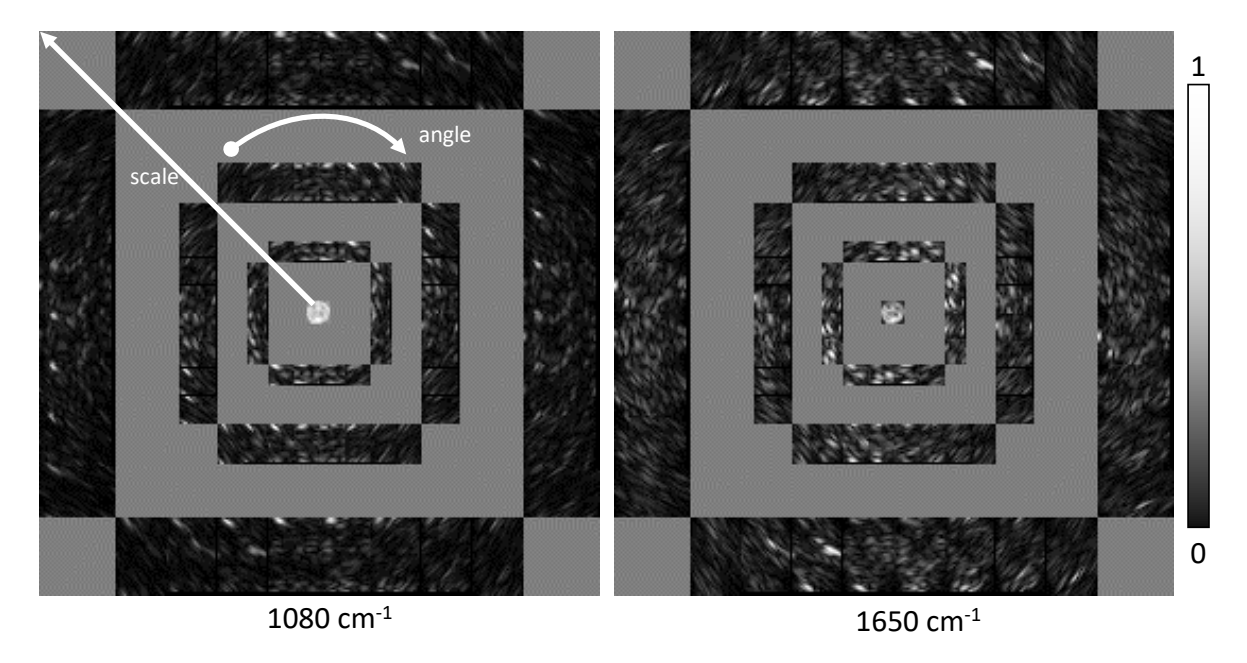


Fig. 2 Curvelet coefficients at four scales for two band images (wavenumber $1080 \mathrm{cm}^{-1}$ and $1650 \mathrm{cm}^{-1}$) from FTIR imaged tissue represented using Cartesian corona. The first coarser scale (low pass filtered) is in the center of the Cartesian concentric corona. Coefficients scale increase from inner corona to the outer corona and at each scale, coefficients at different orientations measured clockwise from the top left.

3.1 Multi-Modal Imaging

27:52:572076775 to total side High side sharing had population (2002 independent of the side of the si

 Both FTIR and dark-field microscopy are used to image unstained tissue cores from breast and ovarian TMAs. Tissue sections were prepared using standard protocols 11 for FTIR imaging. $5\,\mu m$ thick tissue sections from FFPE blocks mounted on IR transparent windows of CaF2 were deparaffinized for imaging, first imaged with FTIR imaging system (Agilent 670 spectrometer coupled to a Cary 620 microscopy system) and then with a dark-field microscope (Nikon Eclipse Ti inverted optical microscope). Agilent Cary 620 FTIR has $15\times0.62\text{NA}$ and 128×128 pixels focal plane array (FPA) detector. We collected mid-IR HS images of tissue sections using standard-definition (SD) mode with $5.5\,\mu m$ pixel size and 8cm^{-1} spectral resolution in the spectral range of 1000 to 3900cm^{-1} .

Tissue sections were imaged with a Nikon inverted optical microscope with a $10\times,0.4$ NA objective in the dark-field mode. A dark-field condenser transmits a hollow cone of light and blocks light from within a disk around the optical axis. In the presence of a sample, scattered light is collected by the objective forming a bright image against a dark background. Based on the Rayleigh criteria, the diffraction-limited spatial resolution of dark-field images collected in the visible range (400 to 700nm) is significantly higher than FTIR images in the fingerprint region (2.5 to 12μ m).

3.2 Pre-processing

In multi-modal fusion, image registration is a critical step, since misalignment can introduce spatial artifacts in the fused result. Both FTIR and dark-field are label-free, enabling multi-modal imaging without additional tissue preparation. This prevents physical distortion of the tissue between images that can lead to misalignment. For this study, we image deparaffinized, label-free tissue sections with both modalities. Multi-modal images were registered by cropping both FTIR and dark-field images to the

same tissue area. We then upsampled FTIR images to match the scale of dark-field images in the *x* dimension. We used the image resize method in OpenCV, using bilinear interpolation to resample each FTIR band image, ³⁸ and OpenCV affine transformations to align dark-field images with FTIR hyperspectral images. ³⁸ Prior to image sharpening, FTIR images underwent standard rubber-band baseline correction to remove scattering artifacts. ³⁹ As baseline correction methods can impact classification, we perform these corrections before spatial frequency injection to facilitate comparison between the original and sharpened images.

3.3 Spatial-Spectral Fusion

In mid-IR imaging, wavenumbers in the *fingerprint* region 900 to $1800 {\rm cm}^{-1}$ are especially important for identifying biomolecules, therefore FTIR hyperspectral images (L) from these wavenumbers are used for histology analysis. The images have a diffraction-limited spatial resolution of 5.5 to $11.11 \mu {\rm m}$. Tissue sections are first imaged with FTIR and then with a dark-field microscope without any intermediate processing.

FTIR data consists of B band images $\mathbf{L}_i \in \mathbf{L}$, where $i=1,\cdots,B$. We performed image sharpening on each band image by fusing spatial features from dark-field image Ψ into \mathbf{L}_i using a curvelet transform algorithm described below. In FTIR, the intensity range in each band varies with absorbance. The range among different bands can vary by a factor of 10. For better image sharpening results, the dark-field image (Ψ) was equalized to Ψ_i for each band image \mathbf{L}_i . Equalization of the dark-field image was performed with linear scaling to match the intensity scale of each band image. The proposed curvelet-based method uses multi-resolution analysis by decomposing each image into a set of spatial features using the fast discrete curvelet transform (FDCT). 37

Higher curvelet coefficients from dark-field image repre-

3

4

5

6

7

8

9 10

11 ∄2

21:52:51202/61/5 21:52:51202/61/5

38

39

40

41

42

43

44

45

46

47

48

49

50

51

52

53

54

55

56

57

58 59 60

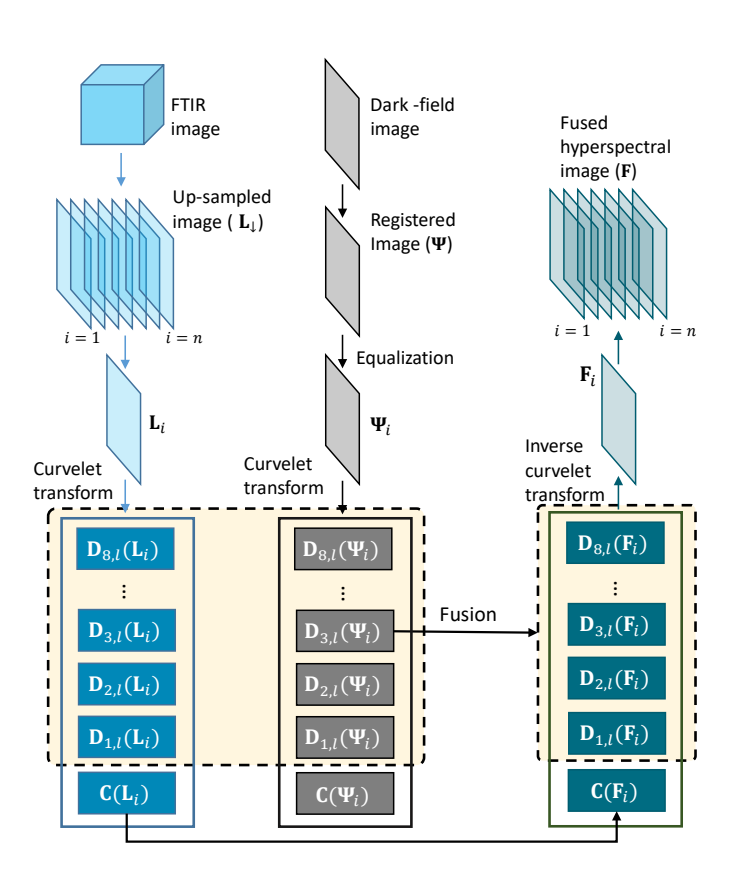


Fig. 3 Process for sharpening broadband low spatial resolution HS images with high spatial resolution dark-field images using the curvelet transform based algorithm. High spatial resolution HS image is obtained by fusing detail coefficients of each low resolution band image with detail coefficients of equalized dark-field image for that band image.

sents sharp features which can be fused in FTIR band images based on Local Magnitude Ratio (LMR). ³⁴ Let $\mathbf{C}_{j,l}(\mathbf{L}_i(x,y))$ and $\mathbf{C}_{j,l}(\mathbf{\Psi}_i(x,y))$ be curvelet coefficients at band \mathbf{L}_i , with the equalized dark-field image $\mathbf{\Psi}_i$ at scale 2^{-j} and orientation l. The LMR at spatial location (x,y) is defined as:

$$LMR_{j,l}(x,y) = \frac{C_{j,l}(\mathbf{L}_i(x,y))}{C_{j,l}(\mathbf{\Psi}_i(x,y))}.$$
 (5)

As the edges in dark-field images are sharper than FTIR data, $LMR_{j,l}(x,y) \leq 1$ at location (x,y) indicates that the spatial details of $\Psi_i(x,y)$ are better than the spatial details of \mathbf{L}_i and therefore are injected into the fused image.

Figure 3 and algorithm 1 illustrate the data fusion process for combining the FTIR hyperspectral image $\bf L$ and registered darkfield image $\bf \Psi$ using curvelet transform.

4 Results

We demonstrate the efficacy and robustness of the proposed technique using two independent datasets consisting of breast and ovarian tissue cores derived from patients at varying stages of cancers. For the sharpened images, we evaluated spatial quality with visual qualitative inspection and assess spectral quality using quantitative metrics. We also compare the performance of curvelet based fusion against PCA based ²⁹ methods.

Algorithm 1 Algorithm for fusing multi-modal images using curvelet transform

- 1. Input: $\mathbf{L} \in \mathbb{R}^{X \times Y \times B}$, $\mathbf{\Psi} \in \mathbb{R}^{X \times Y}$; Output: $\mathbf{F} \in \mathbb{R}^{X \times Y \times B}$
- 2. Select single band image $L_i \in L$, where $i = 1, \dots, B$.
- 3. Compute equalized reference image Ψ_i for L_i .
- 4. Apply fast discrete curvelet transform (FDCT) on L_i and Ψ_i .

$$\mathbf{L}_{c} = \{\mathbf{C}(\mathbf{L}_{i}), \mathbf{D}_{1,l}(\mathbf{L}_{i}), \cdots, \mathbf{D}_{7,l}(\mathbf{L}_{i})\}$$

$$\mathbf{H}_{c} = \{\mathbf{C}(\mathbf{\Psi}_{i}), \mathbf{D}_{1,l}(\mathbf{\Psi}_{i})], \cdots, \mathbf{D}_{7,l}(\mathbf{\Psi}_{i})\}$$

where, \mathbf{L}_c and \mathbf{H}_c are sets of curvelet coefficients of low-resolution band image \mathbf{L}_i and sharp dark-field image $\mathbf{\Psi}_i$ respectively. These coefficients are composed of coarse coefficients $\mathbf{C}(\mathbf{I})$ and detail coefficients $\mathbf{D}_{j,l}(\mathbf{I})$ of image \mathbf{I} at scale 2^{-j} and orientation l.

- 5. Generate curvelet coefficients for fused image i.e. $\mathbf{F}_c = \{\mathbf{C}(\mathbf{F}_i), \mathbf{D}_{1,l}(\mathbf{F}_i), \cdots, \mathbf{D}_{7,l}(\mathbf{F}_i)\}$ using following fusion rules for coarse and detail coefficients.
 - (a) coarse coefficients from \mathbf{L}_c are kept as it is in the fused image

$$\mathbf{C}(\mathbf{F}_i) = \mathbf{C}(\mathbf{L}_i)$$

(b) detail coefficients from \mathbf{L}_c and \mathbf{H}_c are fused using local magnitude ratio (LMR) criteria 34

$$\mathbf{D}_{j,l}\left(\mathbf{F}_{i}(x,y)\right) = \begin{cases} \mathbf{D}_{j,l}\left(\mathbf{L}_{i}(x,y)\right) & \text{if } LMR_{j,l}(x,y) > 1\\ \mathbf{D}_{j,l}\left(\mathbf{\Psi}_{i}(x,y)\right) & \text{if } LMR_{j,l}(x,y) \leq 1 \end{cases}$$

Here, $\mathbf{D}_{j,l}(\mathbf{F}_i(x,y))$ are detail coefficients at scale 2^{-j} and orientation l for fused image \mathbf{F} at spatial location (x,y) and LMR is computed using equation 5.

- 6. Apply inverse FDCT on fused coefficients \mathbf{F}_c to reconstruct the fusion band image \mathbf{F}_i .
- 7. Append fused band image \mathbf{F}_i to generate HS image \mathbf{F}
- 8. Repeat step 2 to 7 for $i = 1, \dots, B$.

Band images of tissue cores from breast TMA AMS 802 are presented in Figure 4, which demonstrates sharpening of the raw FTIR data by fusing high spatial frequency features from the darkfield images of the same cores. Both curvelet and PCA based algorithms sharpen high-frequency features, like fibrous textures or the lining of epithelial cells in lobules. Arrows in the top row point at the fibrous texture in the stromal area, and arrows in the second and third rows (from the top) point to epithelial cells in the terminal duct lobular units (TDLUs) and terminal ducts respectively. Visual inspection of the sharpened images using curvelet based sharpening establishes the improvement in spatial quality as compared to the raw FTIR images. The curvelet-based algorithm also increases spectral localization and avoids adding spectral artifacts during sharpening. However, PCA sharpening fuses spatial details in the raw FTIR data at the cost of greater spectral distortion. Red arrows in PCA sharpened images indicate the loss of spectral information in the fused images due to dominating

View Article Online DOI: 10.1039/D1AN00103E

spatial features from the dark-field images.

2

3

4

5

6

7

8

9

10

11

∄2

38

39

40

41

42

43

44

45

46

47

48

49

50

51

52

53

54

55

56

57

58 59 60 We used three quantitative metrics to evaluate spectral quality which capture distinct characteristics, namely *spectral angle mapper* (SAM), ⁴⁰ histological classification performance metric *area under ROC curve* (AUC) and *classification accuracy* (CA). SAM quantifies the mean angular distance between pixels in a fused image with corresponding pixels in an upscaled raw FTIR image as defined per equation 6 below. SAM values range from (-90, 90) degrees with 0 degree being optimal.

$$SAM(\mathbf{f}_{i}, \mathbf{l}_{i}) = \arccos\left(\frac{\langle \mathbf{f}_{i}, \mathbf{s}_{i} \rangle}{\|\mathbf{f}\| \|\mathbf{s}_{i}\|}\right), \tag{6}$$

where \mathbf{f}_i and \mathbf{l}_i are tissue spectra from fused image \mathbf{F} and upsampled FTIR image \mathbf{L} .

Table 1 Quantitative analysis of image sharpening (breast tissue)

	SAM	AUC	Classification Accuracy
raw	0	0.9831	92%
PCA	2.94	0.9762	91.2%
curvelet	2.22	0.9984	96.7%

Table 2 Quantitative analysis of image sharpening (ovarian tissue)

	SAM	AUC	Classification Accuracy
raw	0	0.9581	91.6%
PCA	1.34	0.9151	89.3%
curvelet	1.21	0.9873	97.6%

Metrics presented in table 1 are computed from 10 tissue cores of 10 different patients at varying stages of cancer. The quantitative results match qualitative image sharpening trends (Figure 4). SAM is typically computed with respect to the ground truth image equation 6. As we cannot directly measure high-resolution HS ground truth images, we estimate SAM using sharpened images with respect to upsampled raw FTIR. SAM values closer to 0 indicate less spectral distortion. Table 1 indicates the average SAM of the proposed curvelet based sharpening algorithm (2.22) is smaller than that for the PCA sharpening algorithm (2.94) for breast tissue cores.

We validated the quality of sharpened (fused) images by analyzing the effect of sharpening on classification performance for histological classes of interest. We were interested in accurate classification of epithelial cells, which are implicated in breast tissue carcinoma. We performed classification of raw FTIR and sharpened HS images for two histology classes: epithelium (green) and stroma (blue) (Figure 5). We used a binary SVM classifier using 12 optimal features selected by the GA-LDA feature selection algorithm ³⁹ and evaluated classification results using two metrics, namely area under the ROC curve (AUC) and classification accuracy. The corresponding results are presented in table 1. The curvelet sharpened images have 1.5% higher AUC and 4.7% higher classification accuracy over the raw FTIR images whereas PCA sharpended images has 0.5% lower AUC and 0.8% lower classification accuracy. The proposed curvelet algorithm

demonstrates superior spectral fidelity compared to PCA because it minimizes spectral distortions.

We assessed the reliability of sharpening results by classifying key histology classes. Raw FTIR images 5(a), PCA sharpened images 5(b), and curvelet sharpened images 5(c) were annotated for two histological classes: epithelium (green) and stroma (blue) using H&E stained adjacent section (5(e)) as the ground truth. A visual comparison of classification images from raw FTIR data 5(f) and curvelet sharpened data 5(h), shows that the 5(h) corresponds more closely to the H&E, especially around the TDLU region as shown in the magnified insets. Several stromal pixels in PCA sharpened images 5(g) are incorrectly classified as epithelial cells due to spectral distortions induced during image sharpening. Our curvelet-based sharpening improves both the sensitivity of epithelial cells and the localization of the cells with sharp edges for lobules that helps precise grading of carcinoma. Misclasssfied pixels are illustrated in figure 6 in red. The curvelet based image 6(d) has fewer misclassified pixels than the raw FTIR image 6(b) and PCA based sharpened image 6(c).

We performed similar extensive analysis for ovarian cancer TMAs (Figure 7 and 8) and observed similar improvements as seen in for breast TMAs. The results are based on total 337982 spectra (149954 for training and 188028 for testing) from 10 tissue cores from different patients at varying stages of cancers. Training and testing spectra are taken from mutually exclusive tissue cores. By testing on spectra from mutually exclusive tissue cores which are measured at different times we have considered spectral measurement uncertainties for imaging settings mentioned here. For this independent dataset, the curvelet sharpened images have 3.0% higher AUC and 6% higher classification accuracy over the raw FTIR images whereas PCA sharpended images have 4.5% lower AUC and 2.4% lower classification accuracy than the raw FTIR images.

Figure 9 compares our sharpened results with O-PTIR (mI-Rage), showing sharpened images of eight ovarian cores from TMA BC11115c. Epithelial cells, stromal cells, adipocytes and lymphocytes are compared with O-PTIR images at the Amide I band (1650cm⁻¹). Qualitative comparison of sharpened images with O-PTIR images indicates that spatial resolution achieved by proposed multi-modal fusion is between FTIR and O-PTIR with spatial details comparable to the optical photothermal imaging.

5 Discussion

The goal of this study was to develop a fast, clinically viable method to enhance image quality by sharpening spatial features in a diffraction-limited mid-IR HS image while preserving spectral fidelity. The proposed multi-modal fusion method requires minimal sample preparation and can fit into a clinical workflow seamlessly. We used rapid, label-free microscopy to augment spatial details in the data from FTIR imaging. Also, being unsupervised, the curvelet based sharpening eliminates the need for super-resolved ground truth images. The results of the proposed image sharpening method are robust and reliable as well as are generally applicable for different tissue types.

The proposed fusion method allows FTIR imaging at larger pixel sizes, thus reducing data collection time. Dark-field mi-

3

4

5

6

7

8

9

10

11

∄2

things of Houston on the control of the control of

38

39

40

41

42

43

44

45

46

47

48

49

50

51

52

53

54

55

56

57

58 59 60 croscopy used in this study is faster than FTIR imaging, therefore, data fusion is a practical solution for improving image quality without increasing data collection time. It takes ≈ 120 minutes to image one tissue core of 1 mm with FTIR in high-definition (HD) mode (pixels size 1.1 μ m) with 16 co-adds, ≈ 3 minutes for the same tissue core with FTIR in SD mode (pixels size $5.5 \mu m$), and $\approx 40sec$ with dark-field microscope. The curvelet transform is implemented using MATLAB and sharpening of a single band image of one tissue core (1059 pixels x 1069 pixels) takes around 6 seconds on a system with 24GB of physical memory and 0.24 seconds with 256GB of physical memory. The proposed fusion method enables roughly 35× faster imaging than the HD mode in FTIR. Data acquisition with larger pixel sizes followed by the application of our algorithm can potentially provide high resolution data with lower collection time and will be explored in the future. Our current instrument limitations have allowed for two pixels sizes: $5.5 \mu m$ (SD imaging mode) and $1.1 \mu m$ (HD imaging mode).

Multi-modal fusion algorithms for image sharpening (pansharpening) can either be supervised or unsupervised. Supervised algorithms require super-resolved ground truth images to find optimization parameters, whereas unsupervised algorithms do not have this requirement. Obtaining super-resolved ground truth in FTIR imaging is challenging because of the diffraction limit. Recent methods ²⁵ for supervised image sharpening have relied on H&E images as a substitute for super-resolved ground truth FTIR data. Since H&E images do not contain spectroscopic information, the algorithm can potentially distort spectral quality in FTIR data by adding wavenumber dependent spatial artifacts to each band image. Our unsupervised method overcomes the challenges encountered by the supervised methods as it does not require super-resolved ground truth images.

In building our classifiers, we performed training and validation on mutually exclusive data in both breast and ovarian cancer TMAs accommodating patient-to-patient variations. Independently processed breast and ovarian tissue TMAs with a diverse array of tissues with varying grades of cancer from different patients reinforces the robustness of our results.

We used two validation metrics Area under ROC curve (AUC) and classification accuracy to evaluate improvement in image quality after sharpening. An ROC curve is a plot of false positive rate vs true positive rate at different thresholds from 0 to 1 for a binary classifier. Higher AUC indicates better classification performance at different thresholds. Overall classification accuracy is a measure of classification performance at an optimal threshold. While quantitative metrics, area under ROC curve (AUC) and classification accuracy, for classification from tables 1 and 2 measure spectral quality of annotated pixels, a qualitative analysis of classification images in breast (figure 5) and ovarian tissue cores (figure 8) helps evaluate spectral fidelity at both annotated and unlabeled pixels, especially in regions important to cancer diagnosis. Qualitative analysis is especially important for the tissue regions with mixed pixels where annotation is challenging. Therefore, we have used a combination of both quantitative and qualitative analyses to evaluate the fidelity of the proposed technique. The superior qualitative and quantitative results demonstrate utility and efficacy of the proposed curvelet based multi-modal fusion method for image sharpening. Both quantitative and qualitative results presented above indicate that image sharpening improves sensitivity and specificity of histological classes, providing a more accurate assessment of the spread of cancer cells in the tissue and in turn facilitates improved understanding of disease prognosis.

We further evaluated image sharpening results by comparing sharpened data with data from O-PTIR images as it provides direct super-resolved images derived from molecular absorbance, which is the same intrinsic parameter measured by FTIR. However, as mechanism for measuring molecular absorbance by O-PTIR is different from FTIR, their absorbance values are not expected to directly match. We therefore compared our results by visual inspection on individual band images from both the datasets.

Higher spectral resolution would increase the computational cost due to an increase in the number of bands. Since the curvelet based fusion operates on individual bands, it allows sharpening of only specific bands based on histological classes of interest. Image sharpening of selected bands reduces the computational time and storage requirement of sharpening the entire HS image with hundreds of bands. This advantage of the proposed method also enables selective enhancement of histological-class-specific morphological features by fusing with other specialized imaging modalities such as second harmonic generation (SHG) imaging for collagen fibers. ^{41,42}

The proposed technique has limitations when the sample under examination has no contrast under a dark field microscope, but consists of chemically distinct species that FTIR imaging recognizes. Here, the algorithm would retain the chemical sensitivity of FTIR imaging but would not improve spatial resolution. For such samples, a different technique (auto-fluorescence, Raman, etc.) which can provide contrast can be used as a substitute for dark-field images. We believe that our algorithm would also work for such image fusion.

6 Conclusion

We describe a novel technique to sharpen diffraction-limited FTIR images and demonstrate improvement in data quality using breast and ovarian cancer tissues. The proposed curvelet based multi-modal fusion technique fuses spatial information from the dark-field images into FTIR hyperspectral images. Each imaging modality contributes complementary information about the sample, therefore, resulting image has the best spatial and spectral information. Also, the curvelet based sharpening is suitable for biomedical images containing curved discontinuities. The proposed technique is both a fast and cost-effective way of enhancing spatial-spectral quality that improves sensitivity and specificity of histological classes deemed important for accurately grading the spread of cancer cells for cancer prognosis.

7 Author contributions

R.M., R.R., D.M., S.P. conceived and planned the experiments. R.M and C.C.G. collected data. R.M., implemented the algorithm, labeled data and carried out experiments. F.F., and S.P., contributed in algorithm implementation R.M., R.R., D.M. analyzed results and prepared the manuscript.

View Article Online DOI: 10.1039/D1AN00103E

Conflicts of interest

There are no conflicts to declare.

Acknowledgements

This work is supported in part by the NLM Training Program in Biomedical Informatics and Data Science T15LM007093 (RM, RR), the Cancer Prevention and Research Institute of Texas (CPRIT) #RR170075 (RR) and #RR140013 (DM), and the National Science Foundation CAREER Award #1943455.

Notes and references

- 1 S. G. Kazarian and K. A. Chan, *Macromolecules*, 2004, **37**, 579–584.
- 2 T. Theophile, *Infrared spectroscopy: Materials science, engineering and technology*, BoD–Books on Demand, 2012.
- 3 A. V. Ewing and S. G. Kazarian, Analyst, 2017, 142, 257-272.
- 4 I. W. Levin and R. Bhargava, *Annu. Rev. Phys. Chem.*, 2005, **56**, 429–474.
- 5 S. Pahlow, K. Weber, J. Popp, R. W. Bayden, K. Kochan, A. Rüther, D. Perez-Guaita, P. Heraud, N. Stone, A. Dudgeon *et al.*, *Applied spectroscopy*, 2018, **72**, 52–84.
- 6 M. J. Baker, E. Gazi, M. D. Brown, J. H. Shanks, P. Gardner and N. W. Clarke, *British journal of cancer*, 2008, **99**, 1859–1866.
- 7 K. Belkebir, P. C. Chaumet and A. Sentenac, *JOSA A*, 2005, **22**, 1889–1897.
- 8 R. K. Reddy, M. J. Walsh, M. V. Schulmerich, P. S. Carney and R. Bhargava, *Applied spectroscopy*, 2013, **67**, 93–105.
- 9 M. J. Nasse, M. J. Walsh, E. C. Mattson, R. Reininger, A. Kajdacsy-Balla, V. Macias, R. Bhargava and C. J. Hirschmugl, *Nature methods*, 2011, **8**, 413–416.
- 10 B. Deutsch, R. Reddy, D. Mayerich, R. Bhargava and P. S. Carney, *JOSA A*, 2015, **32**, 1126–1131.
- 11 M. J. Baker, J. Trevisan, P. Bassan, R. Bhargava, H. J. Butler, K. M. Dorling, P. R. Fielden, S. W. Fogarty, N. J. Fullwood, K. A. Heys et al., Nature protocols, 2014, 9, 1771–1791.
- 12 K. Pandey, *Journal of Applied Polymer Science*, 1999, **71**, 1969–1975.
- 13 A. M. Katzenmeyer, G. Holland, J. Chae, A. Band, K. Kjoller and A. Centrone, *Nanoscale*, 2015, 7, 17637–17641.
- 14 K. A. Chan and S. G. Kazarian, *Chemical Society Reviews*, 2016, 45, 1850–1864.
- A. Dazzi and C. B. Prater, *Chemical reviews*, 2017, **117**, 5146–5173.
- 16 D. Zhang, C. Li, C. Zhang, M. N. Slipchenko, G. Eakins and J.-X. Cheng, *Science advances*, 2016, **2**, e1600521.
- 17 L. C. Grisedale, J. G. Moffat, M. J. Jamieson, P. S. Belton, S. A. Barker and D. Q. Craig, *Molecular pharmaceutics*, 2013, 10, 1815–1823.
- 18 M. Kansiz and C. Prater, Advanced Chemical Microscopy for Life Science and Translational Medicine, 2020, p. 112520E.
- 19 Q. Du, N. H. Younan, R. King and V. P. Shah, *IEEE Geoscience and Remote Sensing Letters*, 2007, 4, 518–522.

- 20 C. Padwick, M. Deskevich, F. Pacifici and S. Smallwood, Proceedings of the ASPRS 2010 Annual Conference, San Diego, CA. USA. 2010.
- 21 D. C. Fernandez, R. Bhargava, S. M. Hewitt and I. W. Levin, *Nature biotechnology*, 2005, **23**, 469–474.
- 22 L. S. Leslie, T. P. Wrobel, D. Mayerich, S. Bindra, R. Emmadi and R. Bhargava, *PLoS One*, 2015, **10**, e0127238.
- 23 J. Du, W. Li, K. Lu and B. Xiao, *Neurocomputing*, 2016, **215**, 3–20.
- 24 K. Kong, C. J. Rowlands, S. Varma, W. Perkins, I. H. Leach, A. A. Koloydenko, H. C. Williams and I. Notingher, *Proceedings of the National Academy of Sciences*, 2013, 110, 15189–15194.
- 25 K. Falahkheirkhah, K. Yeh, S. Mittal, L. Pfister and R. Bhargava, *arXiv preprint arXiv:1911.04410*, 2019.
- 26 A. Garzelli, F. Nencini and L. Capobianco, *IEEE Transactions* on *Geoscience and Remote Sensing*, 2008, **46**, 228–236.
- 27 G. Masi, D. Cozzolino, L. Verdoliva and G. Scarpa, *Remote Sensing*, 2016, **8**, 594.
- 28 P. Kwarteng and A. Chavez, *Photogramm. Eng. Remote Sens*, 1989, **55**, 339–348.
- 29 L. Loncan, L. B. De Almeida, J. M. Bioucas-Dias, X. Briottet, J. Chanussot, N. Dobigeon, S. Fabre, W. Liao, G. A. Licciardi, M. Simoes et al., IEEE Geoscience and remote sensing magazine, 2015, 3, 27–46.
- 30 A. Garzelli, *IEEE Transactions on Geoscience and Remote Sensing*, 2015, **53**, 2096–2107.
- 31 M. Arif and G. Wang, Soft Computing, 2020, 24, 1815–1836.
- 32 V. Bhateja, A. Krishn, A. Sahu *et al.*, Proceedings of the Second International Conference on Computer and Communication Technologies, 2016, pp. 1–9.
- 33 S. AlZubi, N. Islam and M. Abbod, *International Journal of Biomedical Imaging*, 2011, **2011**, 136034.
- 34 C. Rao, J. M. Rao, A. S. Kumar, D. Jain and V. Dadhwal, 2014 IEEE International Advance Computing Conference (IACC), 2014, pp. 952–957.
- 35 G. Pajares and J. M. De La Cruz, *Pattern recognition*, 2004, **37**, 1855–1872.
- 36 D. L. Donoho and A. G. Flesia, *Studies in Computational Mathematics*, Elsevier, 2003, vol. 10, pp. 1–30.
- 37 E. Candes, L. Demanet, D. Donoho and L. Ying, *Multiscale Modeling & Simulation*, 2006, **5**, 861–899.
- 38 P. Joshi, *OpenCV with Python by example*, Packt Publishing Ltd, 2015.
- 39 R. Mankar, M. Walsh, R. Bhargava, S. Prasad and D. Mayerich, *Analyst*, 2018, **143**, 1147–1156.
- 40 L. Alparone, L. Wald, J. Chanussot, C. Thomas, P. Gamba and L. M. Bruce, *IEEE Transactions on Geoscience and Remote Sensing*, 2007, 45, 3012–3021.
- 41 X. Chen, O. Nadiarynkh, S. Plotnikov and P. J. Campagnola, *Nature protocols*, 2012, **7**, 654.
- 42 L. M. van Huizen, N. V. Kuzmin, E. Barbé, S. van der Velde, E. A. te Velde and M. L. Groot, *Journal of biophotonics*, 2019, **12**, e201800297.

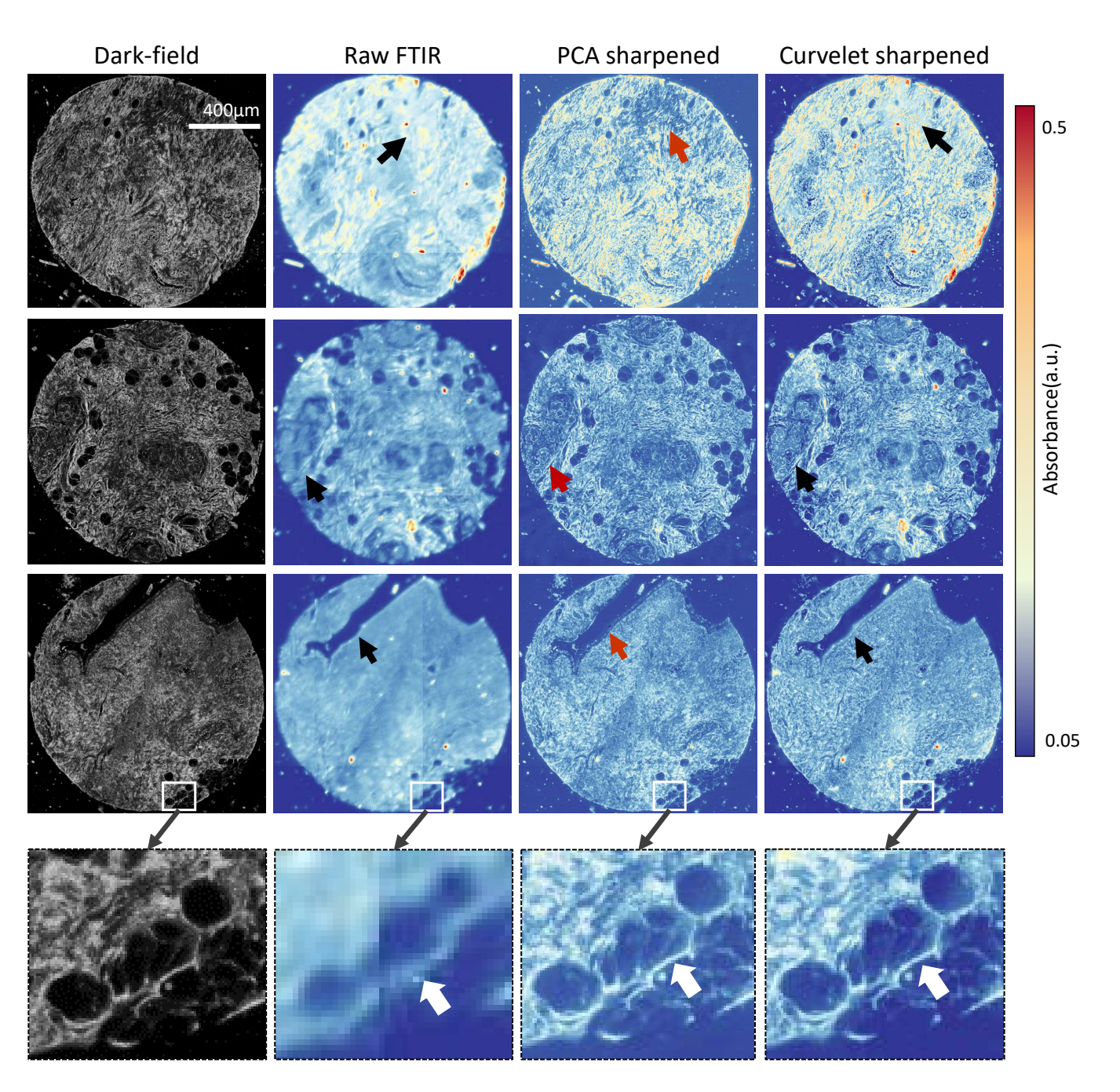


Fig. 4 Multi-modal imaging for improving the spatial resolution of FTIR hyperspectral images using dark field images. The increase in spatial details is observed by comparing raw FTIR images of breast tissue cores with the PCA sharpened images and the curvelet sharpened images at wavenumber 1650cm⁻¹. PCA based sharpening adds spatial details at the cost of spectral information (red arrows). Whereas, proposed curvelet based sharpening can enhance spatial detail while maintaining spectral mapping (black arrows).

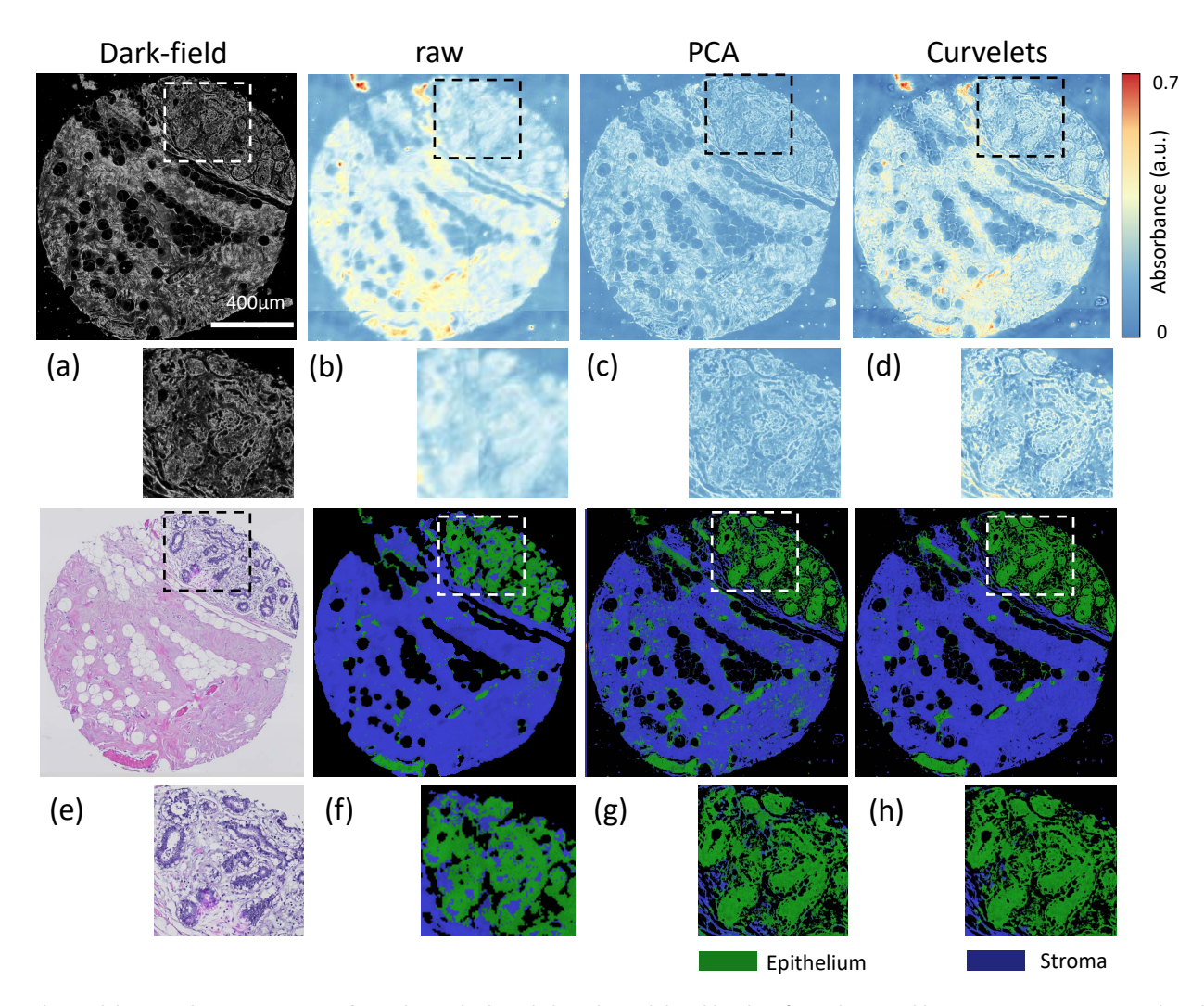


Fig. 5 Multi-modal image sharpening using PCA and curvelet based algorithm validated by classifying sharpened breast tissue cores into two histological classes: epithelium (green) and stroma (blue). Here, first row shows (a) dark-field image and band images at $1650 \, \mathrm{cm}^{-1}$ wavenumber from (b) raw FTIR image, (c) pca based sharpened image and (d) curvelet based sharpened image. Second row shows (e) adjacent section from same breast core stained with hematoxilin and eosin and classified images for (f) raw data (g) pca sharpened data and (f) curvelet sharpened data.

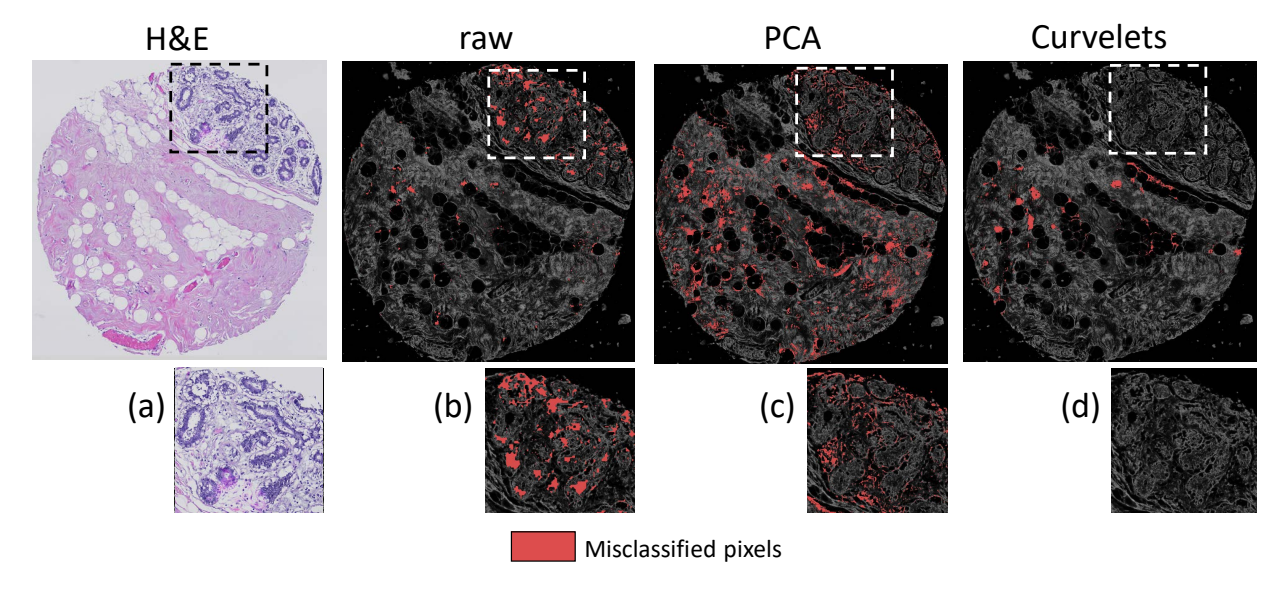


Fig. 6 Effects of image sharpening on classification. (a) H&E stained tissue for ground truth and incorrectly classified pixels are highlighted in red for classification results on: (b) raw FTIR image, (c) PCA based sharpened image and (d) curvelet based sharpened image.

Ma 27:52:573(07)6175 tto indistribution and particular and particular to the position of the particular and particular and particular to the particular and particular and

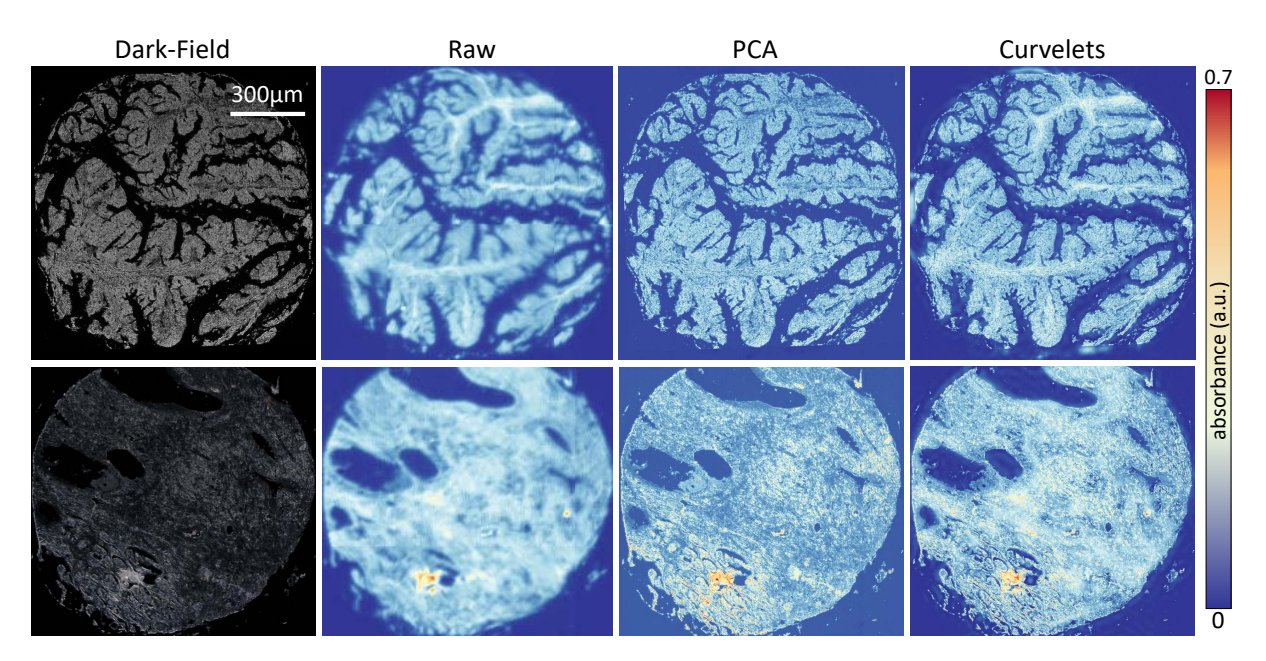


Fig. 7 curvelet based image sharpening with multi-modal imaging is demonstrated using ovarian tissue cores from ovarian TMA BC11115c. Spatial information from dark-field images (left) of ovarian tissue cores is fused to raw FTIR images (middle) used to achieve leveraged spatial resolution in sharpened images (right)

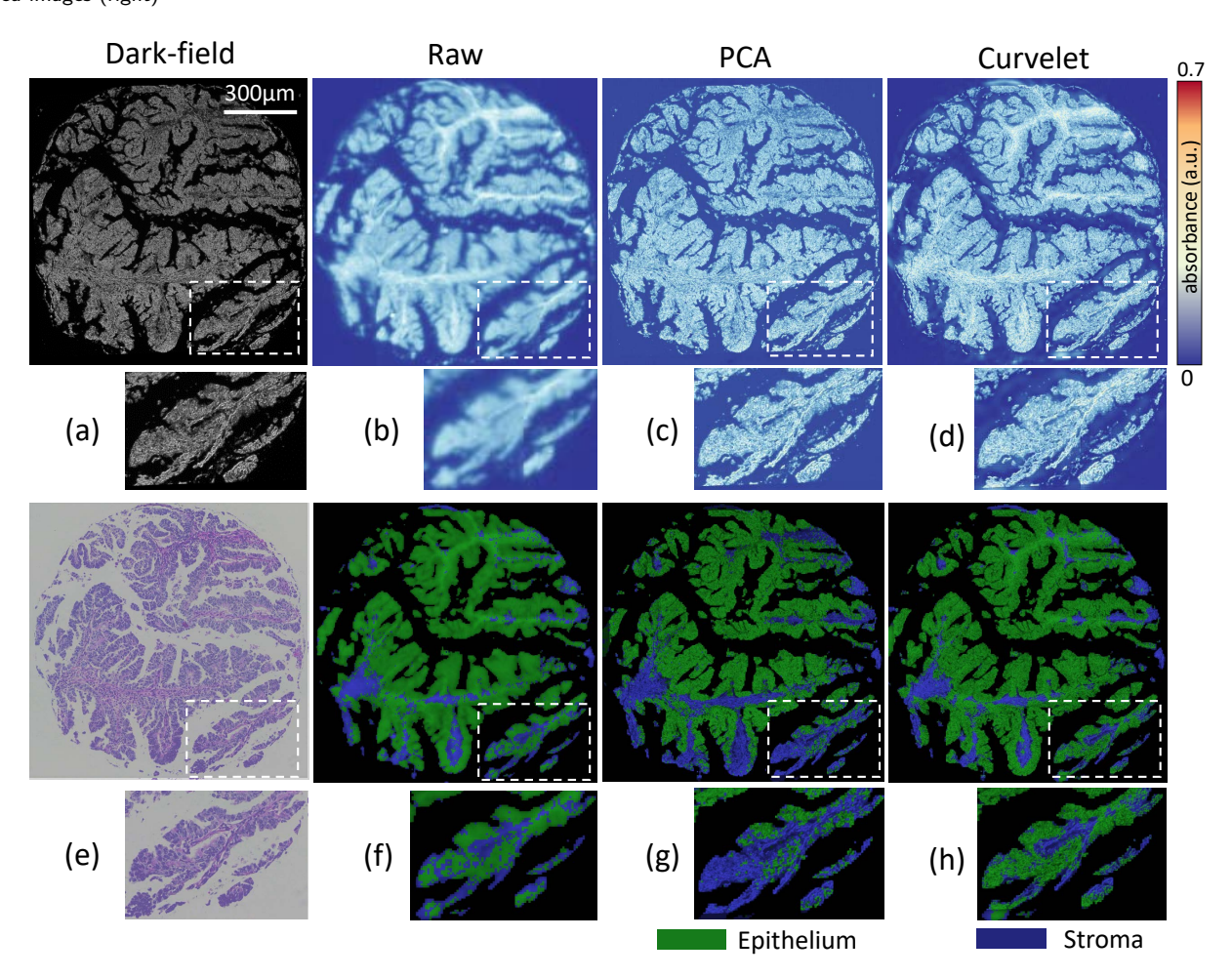


Fig. 8 Qualitative analysis of multi-modal image sharpening using PCA and curvelet based algorithm. Top row: (a) dark-field image, band images at 1650cm⁻¹ wavenumber for (b) raw FTIR image, (c) PCA based sharpened image, and (d) curvelet based sharpened image for the same core. Bottom row: (e) adjacent tissue section stained with hematoxilin and eosin, classified images for (f) raw FTIR image, (f) PCA sharpened image, and (g) curvelet sharpened image which are classified into epithelium (green) and stroma (blue).

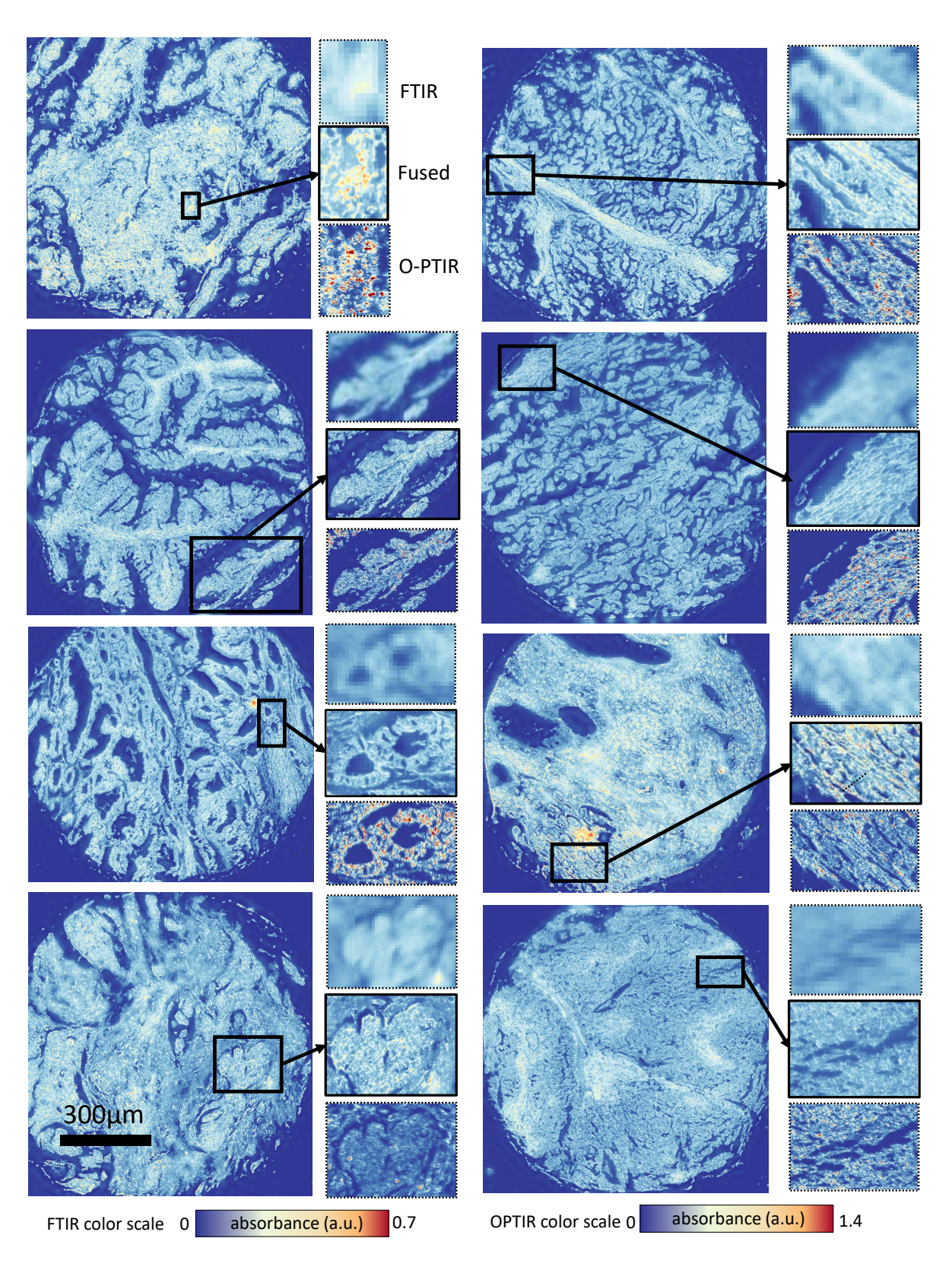


Fig. 9 Image sharpening results on eight ovarian cores from TMA BC11115c with O-PTIR imaging at amide I band (1650cm⁻¹). On the right side of each sharpened (fused) ovarian core image, insets of high frequency features(middle) is compared with raw FTIR (top), and O-PTIR (bottom) images.